

Article

# Design of Inner Ribs with Unequal Stiffness for Deep-Sea Highly Pressure-Resistant Cylindrical Shells and Utilizing NSGA-2 for Lightweight Optimization

Yizhe Huang <sup>1</sup>, Xiao Wang <sup>1</sup>, Zhiqiang Liu <sup>1</sup>, Ying You <sup>1</sup> and Haoxiang Ma <sup>2,\*</sup>

- <sup>1</sup> Hubei Key Laboratory of Modern Manufacturing Quality Engineering, School of Mechanical Engineering, Hubei University of Technology, Wuhan 430068, China; yizhehuang@hbut.edu.cn (Y.H.); 102310162@hbut.edu.cn (X.W.); 102110160@hbut.edu.cn (Z.L.); youying@hbut.edu.cn (Y.Y.)
- <sup>2</sup> Deep Sea Engineering Division, Institute of Deep Sea Science and Engineering, Chinese Academy of Sciences, Sanya 572000, China
- \* Correspondence: mahx@idsse.ac.cn

**Abstract:** For conducting scientific research at depths in the ocean, deep-sea probes are essential pieces of equipment. The cylindrical shell is the most sensible and rational packaging structure for these detectors. New technical challenges for enhancing the pressure resistance and lightweight design of the pressure-resistant cylindrical shell arise from the need to ensure that the detector packaging structure can withstand the immense water pressure at tens of thousands of meters in the underwater environment, while simultaneously reducing the detector packaging structure's self-weight. This article examines the detection system's deep-sea pressure-resistant cylindrical shell. To address the issue of the pressure-resistant shell's insufficient ability to counteract the overall instability caused by the inability to form unstable half-waves in the radial direction when the ring rib pressure-resistant shell experiences it, a design method for the ribs inside the unequal-stiffness pressure-resistant cylindrical shell is suggested. The shell's instability pressure increases by 9.65 MPa following the stiffness adjustment. Simultaneously, in order to attain even more lightweight optimization, the optimal inner rib section was obtained by applying the orthogonal topology optimization method, which also reduced the weight by 106.8 g and effectively improved the compression stability of the high-pressure cylindrical shell structure. Based on this, key optimization variables were found by performing sensitivity analysis on the cylindrical shell structure's parameters. Then, with lightweighting as the primary objective, the high-pressure-resistant cylindrical shell's optimal structural parameters were found using a multi-objective optimization process using the second-generation fast non-dominated genetic algorithm (NSGA-2). This resulted in a weight reduction of 1.2492 kg, or 17.26% of the original pressure-resistant shell. This has led to the development of a lightweight, highly pressure-resistant method for packaging marine exploration equipment structures.



**Citation:** Huang, Y.; Wang, X.; Liu, Z.; You, Y.; Ma, H. Design of Inner Ribs with Unequal Stiffness for Deep-Sea Highly Pressure-Resistant Cylindrical Shells and Utilizing NSGA-2 for Lightweight Optimization. *J. Mar. Sci. Eng.* **2024**, *12*, 1231. <https://doi.org/10.3390/jmse12071231>

Academic Editor: Sergei Chernyi

Received: 28 June 2024

Revised: 18 July 2024

Accepted: 19 July 2024

Published: 21 July 2024

**Keywords:** highly pressure-resistant cylindrical shells; unequal stiffness; orthogonal topology; sensitivity analysis; the second-generation fast non-dominated genetic algorithm; lightweight optimization



**Copyright:** © 2024 by the authors. Licensee MDPI, Basel, Switzerland. This article is an open access article distributed under the terms and conditions of the Creative Commons Attribution (CC BY) license (<https://creativecommons.org/licenses/by/4.0/>).

## 1. Introduction

The ocean is full of resources for human development. However, traditional ocean observation technologies like ship-based observations, ocean buoys, and ocean satellites are no longer able to meet the current needs of ocean exploration due to the urgent need for further in-depth development of underwater resources. For the development of marine resources, high-pressure marine exploration equipment will, therefore, be essential. Submersible detectors come in a variety of shapes and sizes, but they are all made up of three basic parts: a connecting structure, an internal framework platform structure, and a pressure-resistant structure [1–7]. Considering that it makes up between a quarter and a half of the submersible's total weight, the pressure-resistant shell structure is one

of its most important parts. The primary duty of this structure is to tolerate high water pressure from the outside. To achieve the best pressure resistance performance and floating weight ratio, it is crucial to research and optimize the materials and structural forms of pressure-resistant shells.

Reducing the weight or minimizing the total weight of pressure-resistant shells while keeping the necessary strength and stability for operation is the major goal of optimization.

MingYang et al. [8] used the theory of thin shells to build a mechanical model of spherical pressure-resistant shells, which they then used to combine the Penalty Function Method (PFM) with the Multi-Population Genetic Algorithm (MPGA) to optimize the thickness, strengthening ribs, width of the strengthening ribs, and intersection angle of spherical pressure-resistant shells. A. S. Bhanu Prasan et al. [9] also used the PSO algorithm to optimize the quality of an entire pressure-resistant shell under specified buckling pressure and frequency constraints. Muhammad Imran et al. [10] optimized the pressure-resistant shell of a spherical submersible using the genetic algorithm (GA) in ANSYS, and then performed nonlinear buckling analysis on the pressure-resistant shell using a modified RIKS program in ABAQUS. In order to reach the maximum operating depth, Elsayed Fathallah et al. [11] optimized the entire pressure-resistant shell by reducing the elliptical submersible's buoyancy coefficient. The design variables that were utilized were the longitudinal beam size, elliptical radius, and thickness of the pressure-resistant shell, all of which were subject to the limitations of failure criteria and shell buckling strength. Muhammad Imran et al. [12] introduced composite materials into cylindrical pressure-resistant shells, aiming to minimize buoyancy coefficients and maximize buckling load coefficients as optimization research objectives, and executed them through a coupled multi-objective genetic algorithm (MOGA). In order to optimize design variables and obtain the optimal cylindrical pressure-resistant shell, Cheng Wang et al. [13] proposed a cylindrical pressure-resistant shell with non-uniform arch ribs. Based on the parameterization model of the response surface method, they established an approximate model for the output response of ship mass. Honglei Liu et al. [14] proposed an adaptive morphogenesis algorithm based on the growth mechanism of leaf veins. They then applied this method to the design of stiffened plate and shell structures, resulting in a distinct stiffener distribution pattern. Paweł Foryś [15] addressed the impact of geometric defects on the form of equilibrium paths, employed an enhanced particle swarm optimization method (MPSO) for numerical optimization, and utilized the finite element method (FEM) to model and solve cylindrical shell structures. Ghasemi et al. [16] investigated the impact of hydrostatic pressure on cylindrical shells and their preparation by combining a genetic algorithm with geometric, structural, stress, and buckling constraints. Additionally, they used penalty functions to get rid of weak models. In the end, they suggested the best model, taking into account the least amount of weight under pressure. An optimization technique based on a free form was developed by Masatoshi et al. [17] and is especially useful for shape optimization in the out-of-plane direction. The buckling coefficient is the optimization's objective function. The optimization results show that the buckling coefficient can be greatly increased using this method. Wu et al. [18] used the Newton–Lapson iteration method to perform a nonlinear static finite element analysis of axially compressed reinforced cylindrical shell structures with the goal of determining the ultimate load of structural instability. Mahdi et al. [19] optimized the shell and rib parameters under weight and frequency constraints using a genetic algorithm. They also improved the ribs' material composition and shape, and the outcomes demonstrated that the improved shell had superior vibration characteristics. In order to optimize underwater pressure-resistant shells, Akl et al. [20] used a max–min multi-objective optimization strategy. The optimization objectives included shell vibration, noise, and quality. Sofiyev AH et al. [21] introduced the stability of non-uniform nanocomposite cylindrical shells (INCCSs) under hydrostatic pressure in a hot environment. The effective material properties of non-uniform nanocomposite cylindrical shells were modeled based on extended mixing rules. Based on the effective performance of the materials, the basic relationship and stability equation of the thermal environment were derived. The analyt-

ical expressions for the hydrostatic buckling pressure of INCCSs under the framework of FSDT and classical shell theory (CST) were obtained through solutions based on the Galerkin program. Wang M et al. [22] introduced the design and optimization of a pressure cylindrical shell composed of carbon/epoxy resin and glass/epoxy resin composite materials. A method for analyzing composite-pressure cylindrical shells was proposed, and the strength and buckling of composite-pressure cylindrical shells with different rib numbers were analyzed. The effects of thickness and layer angle on critical buckling and strength failure stress were studied. Yang Z et al. [23] used experimental methods to study the buckling pressure and failure strength of non-reinforced fiber-reinforced composite cylindrical shells under external hydrostatic pressure. They collected and discussed strain and pressure data. The results indicate that the improvement in buckling pressure by the ring reinforcement structure is more significant than the increase in failure pressure. The experimental burst pressure of the annular rigid cylindrical shell increased by 23.2%. Zhang X et al. [24] proposed a pressure shell with a corrugated structure to significantly improve its compressive performance. Seven pressure shells were prepared, including six inner corrugated pressure shells and one cylindrical pressure shell, and hydrostatic pressure tests were conducted. The results indicate that the corrugated structure can significantly increase the critical buckling load of the shell. Zhang Y et al. [25] proposed a novel bidirectional corrugated sandwich structure to improve the load-bearing capacity of cylindrical shells. The static and buckling analyses of sandwich shells and unreinforced cylindrical shells with the same volume-to-weight ratio were studied through numerical simulation. The results indicate that the proposed sandwich shell can effectively reduce the ratio of circumferential stress to axial stress from 2 to 1.25, increasing the critical buckling load by approximately 1.63 times. Numerical simulations show that optimizing and adjusting structural parameters can significantly improve the advantages of sandwich shells.

The ultra-high deep-water pressure environment that occurs tens of thousands of meters deep is typically ignored in current research. The standard uniform ribbed method for cylindrical shells may not be able to form unstable half-waves in the radial direction when encountering overall instability in the ultra-deep-water static pressure environment. This could lead to an insufficient ability of the pressure-resistant shell to resist instability. We suggest a technique to modify the internal rib stiffness in order to enhance the pressure-resistant shell's overall anti-instability capabilities in order to address this general instability scenario. However, in terms of lightweight qualities, conventional, ordinary pressure-resistant materials like aluminum alloy 6061T6, resin-based carbon fiber T700, silicon nitride ceramics, etc. cannot be substituted for the titanium alloy TB9 material used to meet the pressure resistance conditions while minimizing volume at depths of tens of thousands of meters. An orthogonal topology optimization method is proposed to further reduce costs by optimizing the inner rib section after adjustment, given the high density and high cost of titanium alloy TB9 material. By combining the second-generation genetic algorithm, NSGA-2, for additional lightweight design in order to obtain the ideal pressure-resistant shell parameters, a multi-objective optimization design of the pressure-resistant shell is also proposed.

In the context of deep-sea high-pressure cylindrical shell structures, the standard uniform ribbed method for cylindrical shells may encounter issues with unstable half-waves in the axial direction when overall instability arises. Additionally, the method is unable to form unstable half-waves in the radial direction, which leaves the pressure-resistant shell with insufficient ability to withstand instability. The idea behind this article is to improve the overall instability resistance of the pressure-resistant shell by adjusting the uneven stiffness of the ribs inside using a method based on the Liz method. This paper suggests using the second-generation fast non-dominated genetic algorithm (NSGA-2) for the multi-objective optimization design of the pressure shell structure in order to obtain the optimal design parameters for the pressure shell. This will allow for the optimization of the inner rib section while maintaining good anti-instability ability and lead to a lightweight design of the entire device.

## 2. Pressure-Resistant Cylindrical Shells with Non-Uniform Internal Ribs Reinforced Structurally

### 2.1. Design of Pressure-Resistant Shell Structure Scheme with Inner Rib Reinforcement Material and Basic Shape Selection for Reinforced Pressure-Resistant Shell with Internal Ribs

The marine environment is harsher and more complex than the terrestrial environment, and it also has many more unknowns for humans. Consequently, given that the pressure-resistant shell in this article operates in an environment that is 10,000 m below the surface, it is part of a strong, high-pressure working environment. The material used to make the pressure-resistant shell should possess qualities like corrosion resistance, light density, and high strength. The pressure-resistant housing’s primary material, titanium alloy TB9, was selected after pertinent processing technology and operating conditions were taken into account. The parameters of commonly used pressure-resistant materials are shown in Table 1 below.

**Table 1.** Mechanical parameters of common materials.

Performance	Structural Steel Q345	Titanium Alloy TB9	Aluminum Alloy 6061T6	Resin-Based Carbon Fiber T700	Silicon Nitride Ceramics	Glass
Elastic modulus (GPa)	210	100	69	120	300	100
Density (g/cm <sup>3</sup> )	7.8	4.5	2.7	1.6	3.2	2.32
Poisson’s ratio	0.28	0.31	0.33	0.3	0.27	0.2
Yield limit (MPa)	345	975	280	600	3820	1450
Specific strength (MPa/(g/cm <sup>3</sup> ))	44	172	104	375	1194	650
Specific rigidity (GPa/(g/cm <sup>3</sup> ))	27	22	26	75	94	45

Current pressure-resistant shells primarily take the shape of regular shapes like ellipsoids, spheres, conics, and cylindrical shapes. Apart from the conventional forms, there exist novel structural variations of pressure-resistant shells, including the ellipsoidal cross-section, lotus root, and corrugated tube.

A spherical pressure-resistant shell’s minimal volume-to-weight ratio and membrane stress are its key benefits, but there are also significant drawbacks. Due to the substantial difference between the spherical pressure-resistant shell’s shape and its streamline, there is a high fluid resistance it encounters when operating underwater, which leads to higher energy consumption. Additionally, the space utilization inside the shell is low and the effective load is small.

With its high space utilization and easy processing, the cylindrical pressure-resistant shell is currently the most popular pressure-resistant shell structure in use worldwide. Based on the dimensions of the sensors needed for this article (as indicated in Figure 1), a cylindrical structure is chosen because the total length of the sensor is approximately 330 mm and it has a long, square shape.

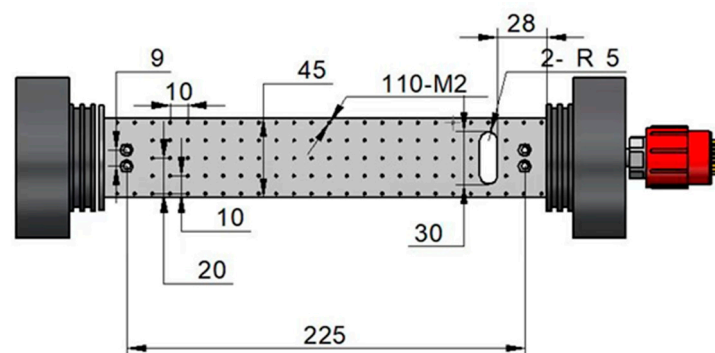


**Figure 1.** Schematic diagram of internal sensor size parameters in the detection system.

## 2.2. Stiffness Distribution Design for the Inner Ribs Using Liz Method

### 2.2.1. A Summary of Inner Rib Rigidity Adjustment Techniques

Currently, pressure-resistant shell reinforced rib sections are primarily designed in rectangular, L-shaped, T-shaped, and I-shaped configurations. The mass of the reinforced rib in the rectangular section is lowest when the section’s moment of inertia is equal. Initially, the shape of the rib section is determined by considering the processing complexity of various types of reinforced ribs. Initially, a rectangle was chosen.

In the study of pressure-resistant shell stiffening technology, the stiffness of each rib is usually considered in an identical manner; this is achieved by selecting the same material and cross-sectional shape for each inner rib. However, there is some logical error in the inner rib positioning. The main reason for this is that the pressure-resistant shell with ring ribs can only form an unstable half-wave in the axial direction when it experiences overall instability; it cannot form an unstable half-wave in the radial direction. This means that the pressure-resistant shell cannot withstand instability very well.

This paper employs the internal rib stiffness allocation technique to address this problem. This technique distributes the stiffness of each rib in accordance with relevant allocation principles, thereby avoiding the instability previously mentioned.

This article’s method for adjusting the stiffness of internal ribs involves modifying the size of the rib section, redistributing the moment of inertia of each rib section, and readjusting the stiffness of every internal rib, all the while maintaining the same number of ribs, rib moments, and total moments of inertia of all the rib sections.

### 2.2.2. Based on the Internal Rib Stiffness Allocation Using the Ritz Method, a Critical Instability Pressure Model for Pressure-Resistant Shells

The critical pressure formula for pressure-resistant shells with inner rib stiffness allocation is derived by applying the Liz method in conjunction with the conventional critical pressure formula for inner ribs with equal stiffness as a reference.

1. The stress of equal-stiffness stiffened pressure-resistant shells can be calculated using this formula.

The following is the main formula used to determine the relevant stress when applying ring ribs to a pressure-resistant shell.

At the midpoint of two ribs and its rib edge, the shell’s normal stress [26] is

$$\begin{cases} \sigma_1 = (\sigma_1)_{x=0} = -\frac{PR}{t}(0.5 \pm \varepsilon_3) \\ \sigma'_1 = (\sigma_1)_{x=0.5l} = -\frac{PR}{t}(0.56 \mp \varepsilon_2) \end{cases} \quad (1)$$

where

- (a)  $\sigma_1$ —at the midpoint of two ribs, the shell plate’s axial normal stress;
- (b)  $\sigma'_1$ —the normal stress axially at the rib’s edge;
- (c)  $P$ —the pressure that the pressure-resistant shell can withstand from the outside.

$$\begin{cases} \sigma_2 = -\frac{PR}{t}(1 - \varepsilon_4 \pm \mu\varepsilon_3) \\ \sigma'_2 = -\frac{PR}{t}(1 - 0.5\mu)(1 - \varepsilon_1) + \mu\sigma'_1 \\ \sigma_2^0 = -\frac{PR}{t}(1 - \varepsilon_4) \end{cases} \quad (2)$$

where

- (a)  $\sigma_2$ —the normal stress around the circumference of two ribs at their midpoint;
- (b)  $\sigma'_2$ —the normal stress circumferential at the rib’s edge;
- (c)  $\sigma_2^0$ —the circumferential normal stress at the midpoint of two ribs on the shell plate.

$$\sigma_f = -E\frac{w_1}{R} = \sigma'_2 - \mu\sigma'_1 = -\frac{PR}{t}(1 - 0.5\mu)(1 - \varepsilon_1) \quad (3)$$

where  $\sigma_f$ —the axial normal stress of ribs.

In accordance with the “Classification and Construction Specification for Submarine Systems and Submarines” [27] requirements, the circumferential normal stress  $\sigma_2^0$  on the middle surface of the shell plate at the midpoint of the two ribs, the axial normal stress  $\sigma_f$  representing the ribs, and the axial normal stress  $\sigma_1'$  at the edge of the ribs must all be verified. The following is the verification formula [26]:

$$\begin{cases} \sigma_2^0 = -\frac{PR}{t}(1 - \varepsilon_4) \leq 0.85\sigma_s \\ \sigma_1' = -\frac{PR}{t}(0.56 \mp \varepsilon_2) \leq 1.15\sigma_s \\ \sigma_f = -\frac{PR}{t}(1 - \varepsilon_1)(1 - 0.5\mu) \leq 0.6\sigma_s \end{cases} \quad (4)$$

2. The Liz method determines the unstable pressure of a pressure-resistant shell and provides instructions for modifying the internal rib stiffness.

The Liz method’s pertinent steps are generally as follows [28]:

- (1) For the internal rib stiffness allocation to the pressure-resistant shell, derive the expression of the instability displacement correlation function. This function must be able to satisfy the boundary conditions and determine the displacement of the ribbed shell deviating from its initial position;
  - (2) Find the expression for the strain and its displacement in different directions at any point in the shell;
  - (3) Determine how the external force work and the shell’s strain energy are related to each other. Then, utilize this expression to determine the expressions for the shell’s total potential energy after deviation, its strain energy, and the external force work;
  - (4) Determine the shell’s stability equation using the principle of minimum potential energy, and then solve for the minimum critical pressure.
3. We calculate the theoretical critical pressure for pressure-resistant shells that have an internal distribution of rib stiffness.

As illustrated in Figure 2, establish a cylindrical coordinate system for the pressure-resistant shell. The graph’s  $\varnothing$  angle indicates the angle formed by the research point’s diameter plane and the reference diameter plane, while the  $x$ -axis direction indicates the pressure-resistant shell’s axial direction.

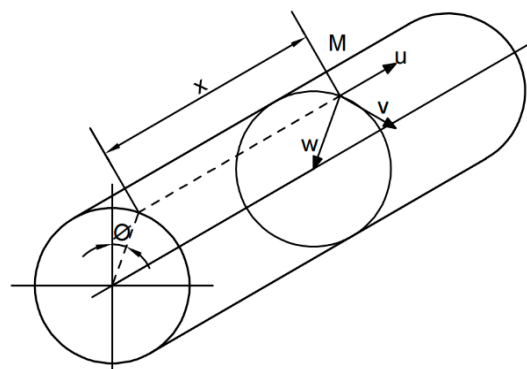


**Figure 2.** Schematic diagram of cylindrical shell’s cylindrical coordinate system.

The deformation at the rigid support and both ends of the shell can be considered continuous when the shell experiences unstable deformation. This continuous deformation can be broken down into axial, tangential, and radial directions [26].

$$\begin{cases} u = A \sin n\varphi \cos \frac{m\pi x}{L} \\ v = B \sin n\varphi \cos \frac{m\pi x}{L} \\ w = C \sin n\varphi \cos \frac{m\pi x}{L} \end{cases} \quad (5)$$

where

- (a)  $L$ —the length of the shell;
- (b)  $m$ —the half-wave number of axial instability when the shell is unstable;
- (c)  $n$ —the whole-wave number of circumferential instability when the shell is unstable;
- (d)  $u$ —the axial displacement of the shell;
- (e)  $v$ —the circumferential displacement of the shell;
- (f)  $w$ —the radial displacement of the shell;  $A$ ,  $B$ , and  $C$  are constants.

With internal rib stiffness allocation, the strain energy of the shell plate for the pressure-resistant shell can be derived as follows, per “Submarine Strength” [27]:

$$\begin{cases} V_1 = \frac{\pi L}{4R} \frac{D}{R^2} \left\{ \begin{aligned} &2(1 - \mu)m^2\alpha^2 + 4(1 - \mu)m^2\alpha^2nBC \\ &+ [(m^2\alpha^2 + n^2 - 1)^2 + 2(1 - \mu)m^2\alpha^2]C^2 \end{aligned} \right\} \\ V_2 = \frac{\pi L}{4R} \frac{Et}{1-\nu^2} \left\{ \begin{aligned} &[m^2\alpha^2 + \frac{1}{2}(1 - \mu)n^2]A^2 + (1 + \mu)mnaAB \\ &+ [n^2 + \frac{1}{2}(1 - \mu)m^2\alpha^2]B^2 + 2nBC + 2\mu m\alpha AC + C^2 \end{aligned} \right\} \\ V = V_1 + V_2 \end{cases} \quad (6)$$

where

- (a)  $V_1$ —shell bending strain energy;
- (b)  $V_2$ —strain energy in the middle surface of the shell,

$$\alpha = \pi R/L.$$

Work of the external force  $U$  [27]:

$$\begin{cases} U_1 = \frac{T_1}{2} \int_0^L \int_0^{2\pi} \left(\frac{\partial w}{\partial x}\right)^2 R d\varphi dx = \frac{\pi L}{4R} T_1 \alpha^2 m^2 C^2 \\ U_2 = -\frac{T_2}{2} \int_0^{2\pi} \int_0^L x_2 w R d\varphi dx = \frac{\pi L}{4R} T_2 (n^2 - 1) C^2 \\ U = U_1 + U_2 \end{cases} \quad (7)$$

In order to determine the internal rib stiffness allocation of pressure-resistant shells, assume that the pressure-resistant shell has a total of  $i$  ribs [26]. Then, the strain energy is  $V_{3i}$ , and the stiffness corresponding to the ribs at  $x_i$  is  $I_i$ .

$$V_{3i} = \frac{EI_i}{2R^3} \pi (n^2 - 1)^2 C^2 \sin^2 \frac{m\pi x_i}{L} \quad (8)$$

It is possible to calculate the strain energy  $V_3$  of the entire pressure-resistant shell rib by adding up the strain energies of each rib [26]:

$$V_3 = \sum_{i=1}^{L/l-1} V_{3i} = \frac{\pi L}{4R} \frac{2E}{R^2 L} (n^2 - 1) C^2 \sum_{i=1}^{L/l-1} (I_i \sin^2 \frac{m\pi x_i}{L}) \quad (9)$$

where  $L$ —the total length of the pressure-resistant shell;

$l$ —rib spacing.

The formula for calculating the total potential energy of the pressure-resistant shell with internal rib stiffness adjustment can be obtained by combining Formulas (7)–(9).

$$\begin{aligned} \Pi = V_1 + V_2 + V_3 - U_1 - U_2 = & \frac{\pi L}{4R} \frac{D}{R^2} \left\{ \frac{2(1-\mu)m^2a^2B^2 + 4(1-\mu)m^2a^2nBC}{\left[ (m^2a^2 + n^2 - 1)^2 + 2(1-\mu)m^2a^2 \right]} C^2 \right\} \\ & + \frac{\pi L}{4R} \frac{Et}{1-\mu^2} \left\{ \begin{aligned} & \left[ m^2a^2 + \frac{1}{2}(1-\mu)n^2 \right] A^2 + (1-\mu)mnaAB \\ & + \left[ n^2 \frac{1}{2}(1-\mu)m^2a^2 \right] B^2 + 2nBC + 2\mu maAC + C^2 \end{aligned} \right\} \\ & + \frac{\pi L}{4R} \frac{2E}{R^2L} (n^2 - 1) C^2 \sum_{i=1}^{L/l-1} \left( I_i \sin^2 \frac{m\pi x_i}{L} \right) - \frac{\pi L}{4R} T_1 a^2 m^2 C^2 - \frac{\pi L}{4R} T_2 (n^2 - 1) C^2 \end{aligned} \tag{10}$$

By removing the high-order trace from the pressure-resistant shell with the internal rib stiffness allocation calculation formula, the stability equation under a uniform external load of the pressure-resistant shell with internal rib stiffness allocation can be obtained by replacing it with the basic relationship formula of the Liz method [26]:

$$T_1 m^2 a^2 + T_2 (n^2 - 1)^2 = \left\{ \begin{aligned} & \frac{D}{R^2} (n^2 - 1 + m^2 a^2) + \frac{Et m^4 a^4}{n^2 + m^2 a^2} \\ & + \frac{2E}{R^2 L} (n^2 - 1)^2 C^2 \sum_{i=1}^{L/l-1} \left( I_i \sin^2 \frac{m\pi x_i}{L} \right) \end{aligned} \right\} \tag{11}$$

Under uniform pressure P, the transverse and longitudinal sections of the pressure-resistant shell experience initial membrane forces denoted by  $T_1$  and  $T_2$  in the equation above. It can be roughly described as follows, generally:

$$\left. \begin{aligned} T_1 &= 0.5PR \\ T_2 &= PR \end{aligned} \right\} \tag{12}$$

Formulas (11) and (12) can be combined to obtain the following theoretical critical pressure calculation formula for the overall instability of pressure-resistant shells with internal rib stiffness allocation:

$$P_E = \frac{1}{n^2 - 1 + 0.5m^2 a^2} \left[ \begin{aligned} & \frac{D}{R^3} (n^2 - 1 + m^2 a^2)^2 + \frac{Et}{R} \frac{m^4 a^4}{n^2 + m^2 a^2} \\ & + \frac{2E}{R^3 L} (n^2 - 1)^2 \sum_{i=1}^{L/l-1} \left( I_i \sin^2 \frac{m\pi x_i}{L} \right) \end{aligned} \right] \tag{13}$$

where  $m$ —the number of half-waves formed upwards when the pressure-resistant shell buckles;

$n$ —the number of half-waves formed by the circumferential instability of the pressure-resistant shell.

### 2.2.3. Examining the Critical Instability Pressure of Cylindrical Shells with Adjustable Internal Rib Stiffness

The pressure-resistant shell has six evenly spaced ribs and measures  $L = 350$  mm in total length,  $D = 90$  mm in inner diameter, and  $t = 5$  mm in thickness. The rib width is 5 mm, rib spacing is 50 mm, and rib thickness is 3 mm. The chosen material is titanium alloy TB9, with associated characteristics including elastic modulus  $E = 100$  GPa, yield limit  $\delta_s = 975$  MPa, Poisson’s ratio  $\mu = 0.31$ , and an applied load of 10 MPa.

The main calculation process is as follows:

1. Calculate the total moment of inertia of the ribs.

According to the Chinese CCS submersible design specifications, the formula for calculating the moment of inertia  $I$  of the ribs with plates is as follows [26]:

$$I = I_0 + \frac{lt^3}{12} + \left( y_0 + \frac{t}{2} \right)^2 \times \frac{ltF}{lt + F} \tag{14}$$



where

- (a)  $I_0$ —the moment of inertia of each rib section;
- (b)  $F$ —the rib cross-sectional area;
- (c)  $y_0$ —the distance from the axis of the rib section to the middle surface of the shell;
- (d)  $t$ —the thickness of pressure-resistant shell;
- (e)  $l$ —the rib spacing.

The rib section with plates' moment of inertia can be computed as  $I = 7166.91 \text{ mm}^4$  using Formula (14).  $I_{total} = 43001.46 \text{ mm}^4$  is the rib section's total moment of inertia with six plates.

2. Determine the radial displacement ratio at which each unstable rib occurs.

When an instability occurs in a cylindrical shell, the shell plate's radial displacement exhibits a trend of progressive decrease on both sides. The formula for radial displacement is as follows:

$$w = C \sin(n\varphi) \sin\left(\frac{m\pi x}{L}\right) \tag{15}$$

3. Reassign the stiffness of each rib.

Redistribute each rib section's moment of inertia after utilizing Formula (15) to determine the radial displacement ratio between each rib. The following formula applies in this case:

$$I_i = \frac{\sin\left(\frac{m\pi x_i}{L}\right)}{\sum_{i=1}^6 \sin\left(\frac{m\pi x_i}{L}\right)} I_{total} \tag{16}$$

In the formula:  $I_i$ —the stiffness of each rib.

Each rib's assigned stiffness can be computed after completing the aforementioned three steps. Each rib's parameters are displayed in Table 2, where changing the rib thickness while keeping the rib width the same allows for the adjustment of each rib section's moment of inertia.

**Table 2.** Distribution of moment of inertia of rib section.

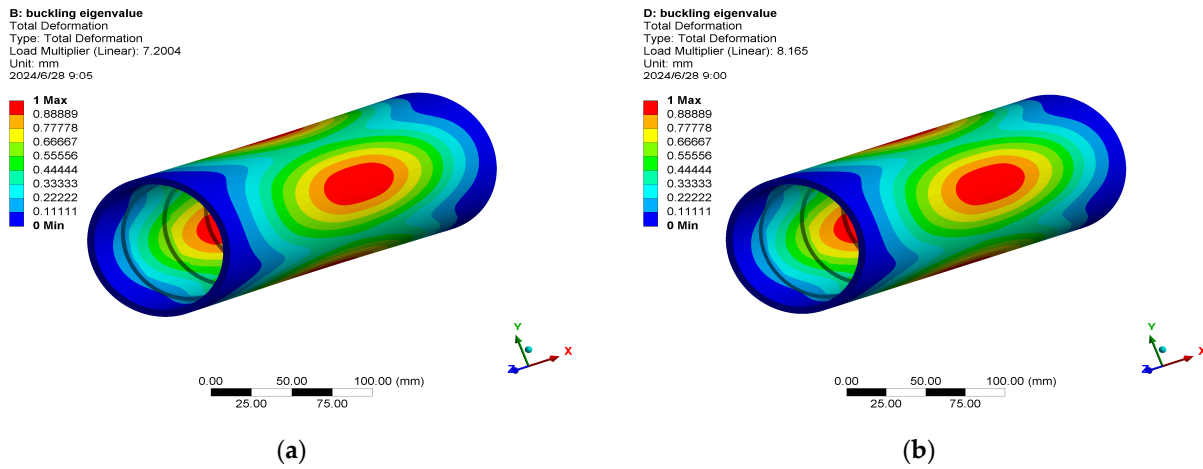
Rib Number	1 and 6	2 and 5	3 and 4
Inertia of rib section with plate/mm <sup>4</sup>	4902.17	6923.24	9675.33
Rib height/mm <sup>4</sup>	2.643	2.966	3.316

Through the substitution of the rib section's moment of inertia from Table 1 into Formula (13), the pressure-resistant shell's overall instability critical pressure  $P_{E1}$  with inner rib stiffness allocation is 79.68 MPa, while the pressure-resistant shell's overall instability critical pressure  $P_{E2}$  with equal stiffness is 70.24 MPa.

2.2.4. Analyzing Cylindrical Shells through Simulation with Adjustable Internal Rib Stiffness

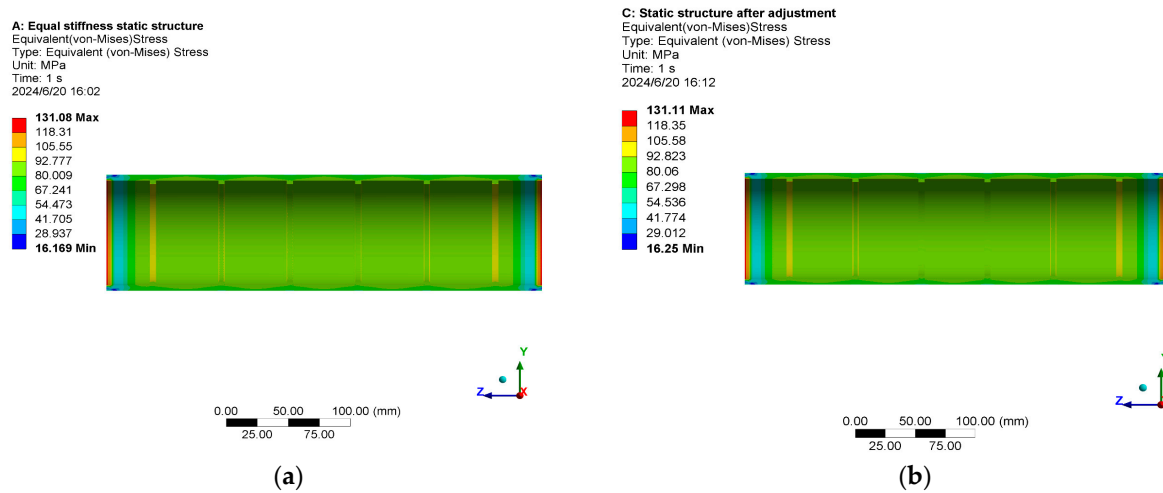
The equal-stiffness internal rib shell pressure,  $P_{E2}$ , and the overall instability critical pressure,  $P_{E1}$ , were obtained in the previous section using the internal rib stiffness adjustment theory's critical instability pressure calculation formula. ANSYS Workbench 2023 R1 software was used to perform the pertinent simulation calculations discussed in this section. The grid was set as a hexahedral grid with a grid size of 1 mm. The convergence process of the grid was automatically determined by the program, with fixed constraints at the two circular rings on the cylindrical surface. The pressure was set to 10 MPa on both sides of the cylinder. The accuracy of the theoretical formula was confirmed by comparing the obtained results with the theoretical values. At the moment, the most popular approach for researching structural stability is linear buckling analysis. Its primary feature, which is a finite element analysis, is to treat the entire structure as an elastic structure and ignore the original defects of the structure itself [29].

Figure 3 displays the characteristic values of the buckling deformation analysis obtained after the internal rib stiffness of the pressure-resistant shell was adjusted through ANSYS Workbench simulation calculations.



**Figure 3.** Eigenvalue buckling analysis deformation diagram. (a) Instability mode of shell with equal stiffness and inner ribs; (b) instability mode of inner rib stiffness adjustment shell characteristics.

We obtained the Mises stress cloud maps that are pertinent, as illustrated in Figures 4 and 5.



**Figure 4.** Mises shell stress cloud maps: (a) Mises stress cloud map of the inner rib cage with the same degree of rigidity; (b) the inner rib stiffness adjustment shell’s Mises stress cloud map.

From the above results, it is evident that the maximum stress on the ribs is 96.753 MPa and the maximum stress on the equal-stiffness inner rib pressure-resistant shell is 131.08 MPa. The critical instability pressure in the first-order instability state is 72 MPa, which is represented by the buckling characteristic value of 7.2. The inner rib stiffness-adjusted pressure-resistant shell can withstand stresses up to 131.11 MPa, while the ribs themselves can withstand stresses up to 96.975 MPa. The first-order instability state has a buckling characteristic value of 8.165, which is equivalent to a critical instability pressure of 81.65 MPa. This confirms the accuracy of the theoretical formula for critical instability pressure derived in this article. It can be seen that the critical instability pressure in both simulation results is essentially consistent with the critical instability pressure calculated using the derivative theory formula in the previous section.

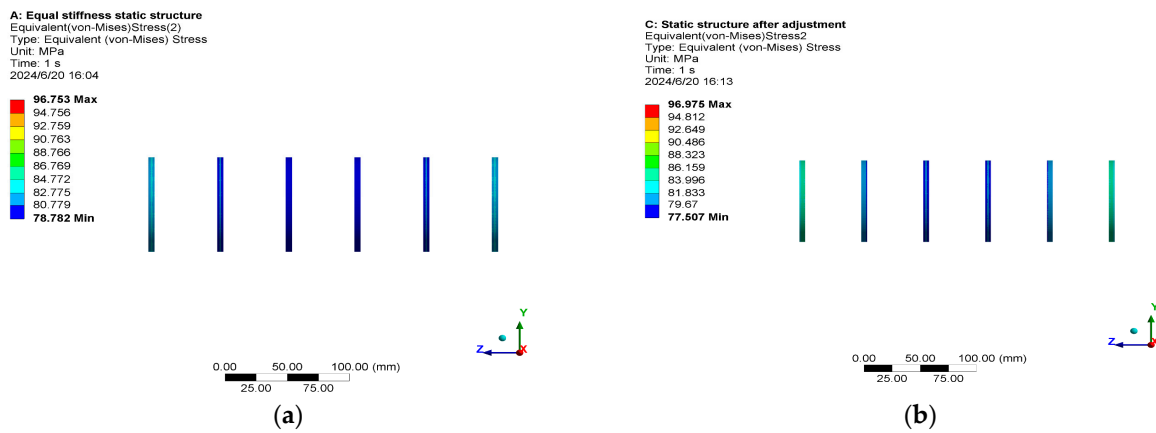


**Figure 5.** Mises stress cloud maps of ribs: (a) Mises stress cloud map of ribs with equal stiffness; (b) Mises stress cloud map for rib stiffness adjustment.

In terms of stability, the instability pressure of the inner rib stiffness adjustment method is 9.65 MPa higher than that of the inner rib with equal stiffness, despite the two stiffening methods having similar maximum stresses. Increasing the internal rib stiffness can boost the pressure-resistant shell’s compressive strength and stability, as can be observed.

### 2.3. Optimization of the Inner Rib Reinforcement Cross-Sectional Orthogonal Topology Using the Variable Density Approach

#### 2.3.1. Design Strategy for Orthogonal Topology Optimization

With the maximum stress of the optimized strengthening rib as the primary optimization objective and the number of iterations needed for topology optimization as the second evaluation indicator, the goal is to obtain the cross-sectional shape of the strengthening rib with the strongest compressive strength. The variable density method is used to optimize the orthogonal topology of the rib’s cross-sectional shape. As a design variable, the range of relative element material density  $\rho$  in the optimization region is defined as [0, 1]. The pressure-resistant shell’s minimum weight serves as the objective function, and its maximum stress and maximum strain are set as constraint conditions. Formula (17) [30,31] illustrates how the relative element material density  $\rho$  represents the objective function in the mathematical model of the variable density method topology optimization.

$$\begin{aligned}
 find(\rho) &= (\rho_1, \rho_2 \dots, \rho_n) \\
 minm(\rho) &= \int_V \rho dV \\
 s.t \left\{ \begin{aligned}
 E(\rho_i) &= \rho_i^P E_0 \\
 \int_V \rho dV &\leq M^* (i = 1, 2 \dots, n) \\
 0 &\leq \rho_{min} < \rho_i \leq 1
 \end{aligned} \right. \tag{17}
 \end{aligned}$$

where

- (a)  $\rho$ —the relative density of the unit materials, one of the design variables;
- (b)  $m(\rho)$ —the optimized design area’s quality, represented by the objective function;
- (c)  $V$ —the volume occupied by the design area;
- (d)  $E(\rho_i)$ —the relative density of unit materials, represented by the relative elastic modulus;
- (e)  $P$ —the penalty factor;
- (f)  $E_0$ —the material’s true elastic modulus;
- (g)  $M^*$ —the optimized quality’s maximum value;
- (h)  $n$ —maximize the quantity of limited components within the design domain;
- (i)  $\rho_{min}$ —the lowest relative density of the material in question.

Grid size  $t$ , penalty factor  $p$ , and volume factor  $f$  are the primary variables influencing the outcomes of topology optimization. We should prevent checkerboard phenomena, porosity, and non-convergence during the topology optimization process and accurately depict the structure’s mechanical characteristics. The selections in this article are  $0.3 \leq f \leq 0.7$ ,  $3 \leq p \leq 5$ , and  $0.5 \text{ mm} \leq t \leq 1 \text{ mm}$ .

The volume factor  $f$ , penalty factor  $p$ , and grid size  $t$  are the primary factors influencing the optimized object’s performance in terms of pressure resistance, as was observed in the previous step. The three parameters mentioned above are denoted as factors A, B, and C, respectively. It is presumed that there is no interplay among the three factors [32]. As indicated in Table 3, the level of factors for orthogonal topology optimization experiments is established based on the range of values for each factor suggested in the preceding text, as well as comparable research and design experience.

**Table 3.** Orthogonal experimental factor level table for three parameters.

Horizontal	Volume Coefficient (A)	Penalty Factor (B)	Grid Size (C)
1	0.4	2.0	0.5
2	0.5	3.0	0.75
3	0.6	4.0	1.0

Based on this, the orthogonal experimental table needed for the experiment is shown in Table 4 (note that this article only contains three horizontal factors; therefore, a standard orthogonal table would require the addition of a set of blank factors).

**Table 4.** Orthogonal topology optimization experimental scheme combination table.










Test Number	Volume Coefficient (A)	Penalty Factor (B)	Grid Size (C)	Blank (D)
1	0.4	2.0	0.5	-
2	0.4	3.0	0.75	-
3	0.4	4.0	1	-
4	0.5	2.0	0.75	-
5	0.5	3.0	1	-
6	0.5	4.0	0.5	-
7	0.6	2.0	1	-
8	0.6	3.0	0.5	-
9	0.6	4.0	0.75	-

### 2.3.2. Test Results and Analysis

#### Test Result

Table 5 displays the pertinent results of the topology optimization based on the variable density method that was carried out using ANSYS Workbench on the nine experiments that were previously mentioned. In topology optimization settings, the mesh is a hexahedral mesh, and the mesh size was automatically selected based on the parameters in Table 5. The mesh convergence process was automatically determined by the program, and the pressure was set to a uniform distribution of 10 MPa on the outer ring of the circular ring. At the same time, cylindrical support was applied to the outer ring, and free constraints were given in the radial direction.

**Table 5.** Comparing cross-sectional topological forms with various combinations of parameters.

Test Number	1	2	3	4	5	6	7	8	9
Combination number	$A_1B_1C_1$	$A_1B_2C_3$	$A_1B_3C_3$	$A_2B_1C_2$	$A_2B_2C_3$	$A_2B_3C_1$	$A_3B_1C_3$	$A_3B_2C_1$	$A_3B_3C_2$
Cross-sectional figure									
Maximum stress (MPa)	267.74	285.59	259.47	241.85	259.24	269.01	221.72	239.14	249.34
Iteration steps	18	13	12	18	13	15	16	15	16

Range Analysis of Experimental Results

The range analysis table for this experiment is displayed in Table 6. In the table,  $K_i (i = 1, 2, 3)$  denotes the average value of the test results corresponding to level  $i$ , and  $k_i$  represents the sum of the test results corresponding to level  $i$  in any column. Making a relationship graph between various levels and target parameters to aid in comprehension of how different level factors affect target parameters is also practical, and is shown Figure 6.

Table 6. (a) Range analysis table for maximum stress. (b) Range analysis table for iteration steps.

(a)					
Experimental Indicators	Test Number	A Volume Coefficient	B Penalty Factor	C Mesh Size	D Blank
Maximum stress	$K_1$	812.8	731.31	775.89	776.32
	$K_2$	770.1	783.97	776.78	776.32
	$K_3$	710.2	777.82	740.43	740.46
	$k_1$	270.93	243.77	258.63	258.77
	$k_2$	256.7	261.32	258.93	258.77
	$k_3$	236.73	259.27	246.81	246.82
	Range R	34.20	15.50	12.12	11.95
Primary and secondary order			A > B > C > D		
Excellent level		A <sub>3</sub>	B <sub>1</sub>	C <sub>3</sub>	D <sub>3</sub>
Optimal combination		A <sub>3</sub> B <sub>1</sub> C <sub>3</sub>			
(b)					
Experimental Indicators	Test Number	A Volume Coefficient	B Penalty Factor	C Mesh Size	D Blank
Iteration steps	$K_1$	43	52	48	47
	$K_2$	46	41	47	44
	$K_3$	47	43	41	45
	$k_1$	14.33	17.33	16	15.67
	$k_2$	15.33	13.67	15.67	14.67
	$k_3$	15.67	14.33	13.67	15
	Range R	1.33	3.67	2.33	1
Primary and secondary order			B > C > A > D		
Excellent level		A <sub>3</sub>	B <sub>1</sub>	C <sub>3</sub>	D <sub>3</sub>
Optimal combination		A <sub>1</sub> B <sub>2</sub> C <sub>3</sub>			

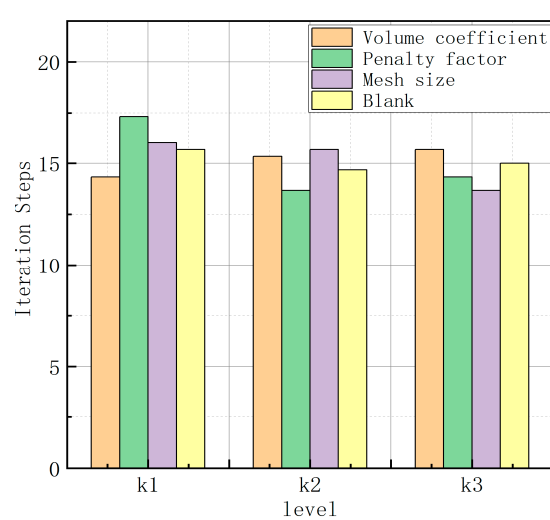
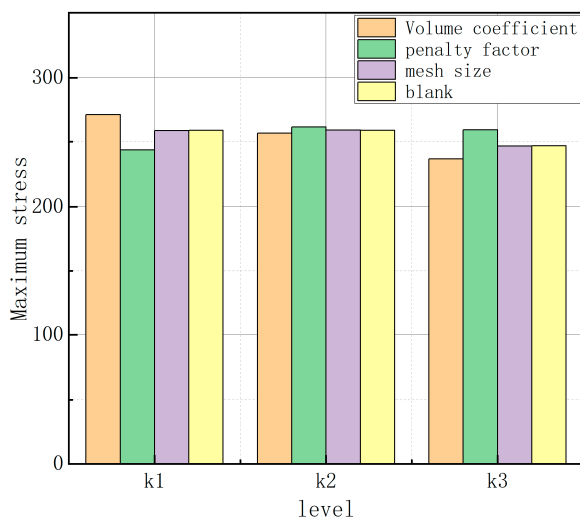


Figure 6. Diagrams of relationships between assessment indicators and various levels. (a) The relationship between different levels and maximum stress; (b) the relationship between different levels and iteration steps.

The analysis presented above leads to the conclusion that the volume coefficient has the greatest influence on the maximum stress evaluation index, whereas the grid size has the least influence. The number of iteration steps is primarily determined by the penalty factor, with the volume coefficient having the least significant effect. The combinations of  $A_3B_1C_3$  and  $A_1B_2C_3$ , respectively, represent the ideal solutions that correspond to the two evaluation indicators of maximum stress and iteration steps. With a maximum stress of 221.72 MPa and 16 iteration steps,  $A_3B_1C_3$  is present in the aforementioned experiment (as indicated by the pertinent simulation figure in Figure 7). Nevertheless, additional testing is required because  $A_1B_2C_3$  was not randomly identified in the orthogonal experiment. The pertinent findings are displayed in Figure 8. The maximum stress following  $A_1B_3C_3$  combination optimization is 285.59 MPa, and 12 iteration steps were used.

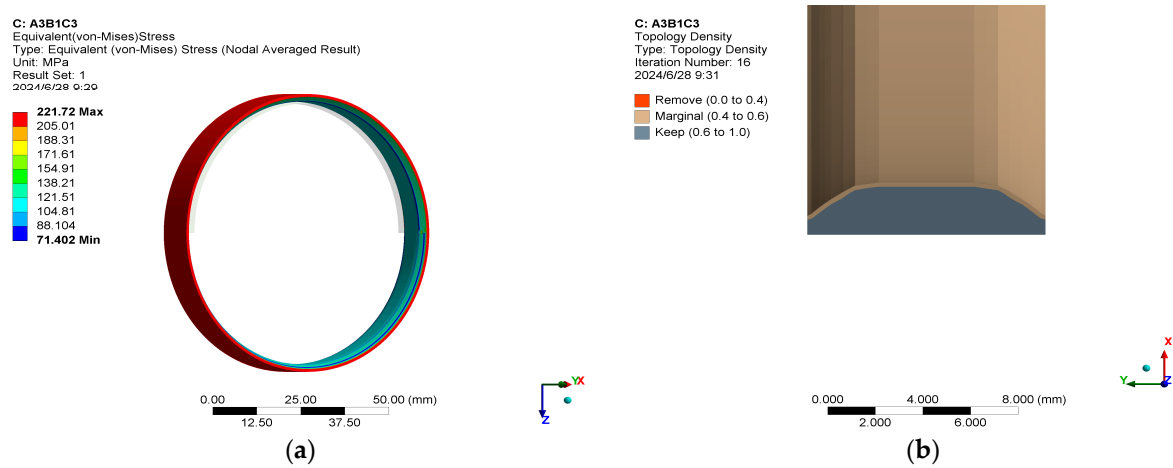


Figure 7. Maximum stress cloud and section diagram after optimizing  $A_3B_1C_3$  combination. (a) Maximum stress cloud map; (b) cross-section view.

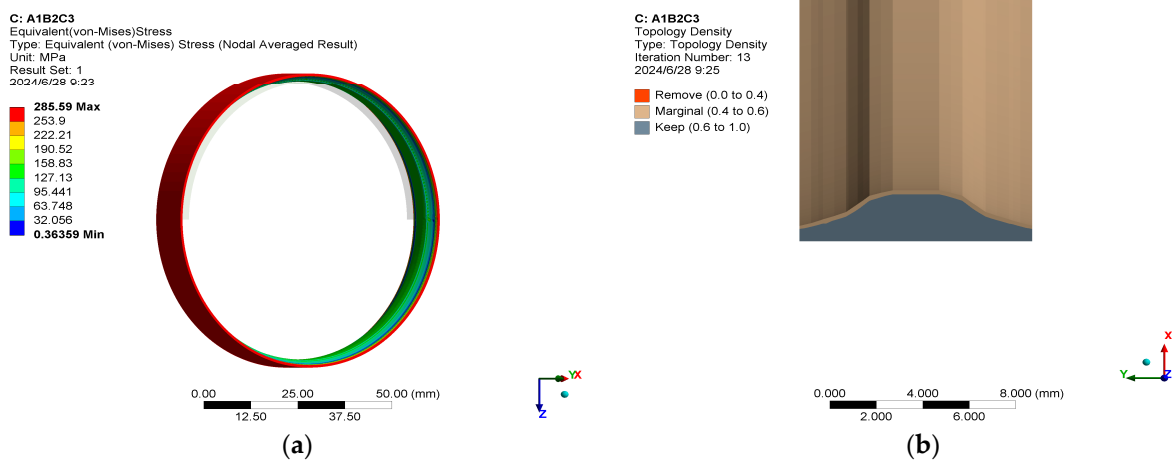


Figure 8. Maximum stress cloud and section diagram after optimizing  $A_1B_2C_3$  combination. (a) Maximum stress cloud map; (b) cross-section view.

When the maximum stress of the  $A_3B_1C_3$  scheme is compared to the  $A_1B_2C_3$  scheme, it is 63.87 MPa less. The optimization process requires four more iterations for the  $A_3B_1C_3$  scheme than for the  $A_1B_2C_3$  scheme. But since achieving high pressure resistance is the primary goal of this article, it was ultimately determined that  $A_3B_1C_3$ , with a volume factor of 0.6, a penalty factor of 3, and a grid size of 1 mm, is the best combination for cross-sectional topology optimization.

### Analysis of Optimization Results

Subsequent manufacturing processes encounter certain challenges because of the optimized cross-section's uneven and multiplanar edges. Post-processing procedures are therefore required to guarantee that the optimized model can be produced and processed with ease. Figure 9 displays the model's processed rib section following imitation optimization. The rib section is referred to in this article as having a bow-like shape because of its shape.



**Figure 9.** Outline drawings of reinforced rib section after processing: (a) 3D schematic diagram of strengthening ribs; (b) 2D schematic diagram of strengthening ribs.

Table 7 displays the information pertaining to the modeling and simulation analysis of the optimized bow section.

**Table 7.** Comparison table of data from different cross-sections.

	Maximum Stress/MPa	Maximum Displacement/mm	Mass/g
Reinforced ribs with rectangular cross-section	160.20	0.670	37.88
Strengthening ribs of the original bow section	221.72	0.105	20.43
Reinforced rib of processed arched section	199.51	0.084	25.45

The stress dropped from 221.72 MP to 199.51 MP, a decrease of 22.21 MPa, even though the processed section's mass increased by 5.02 g in comparison to the untreated reinforcing ribs. A weight reduction of 12.43 g (24.89%) and 106.8 g (the total weight of the six ribs) over the original rectangular section allowed for some partial fulfillment of the lightweight requirement.

The internal rib stiffness adjustment method described in the previous section was applied to the obtained section of the arched rib. Sequentially, we numbered the ribs from left to right. B1 is the formula for rib 1's width, and so forth. Ribs 2, 3, 4, 5, and 6 have widths of  $b_2$ ,  $b_3$ ,  $b_4$ ,  $b_5$ , and  $b_6$ , in that order. The different parameters of the rib cross-section will be defined as follows, as shown in Figure 10, where  $h = b/10$  and  $c = b/5$ , to guarantee that the cross-sectional shape of the ribs does not change.

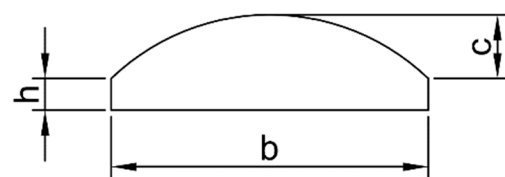


**Figure 10.** Definition diagram of arched rib parameters.

A formula was used to determine each rib section’s moment of inertia, and the results are displayed in Table 8.

**Table 8.** Related parameters of ribs.

Number	Inertia Moment of Rib Section with Plate/mm <sup>4</sup>	Cross-Section Area/mm <sup>2</sup>	Rib Width/mm	Rib Height/mm
1 and 6	5633.388	19.67	9.1	2.73
2 and 5	7955.925	23.33	9.91	2.97
3 and 4	11118.53	27.6	10.78	3.23

The three-dimensional schematic diagram is shown in Figure 11.

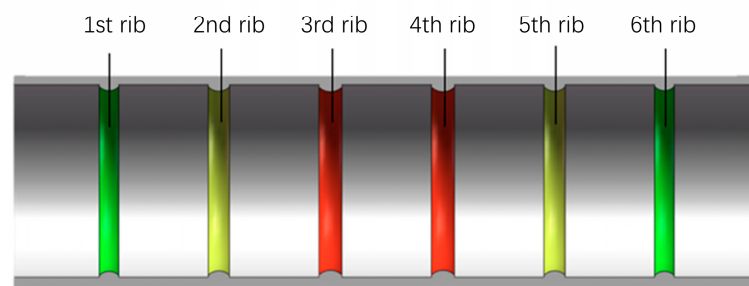


**Figure 11.** Cross-section diagram of pressure-resistant shell.

Finally, as indicated in Table 9, the initial parameters of the complete cylindrical pressure shell structure were obtained.

**Table 9.** Initial shell-related data.

Name	Number	Unit
Shell length	350	mm
Shell thickness	5	mm
Inner diameter of shell	90	mm
Front bulkhead width	45	mm
Rear bulkhead width	45	mm
Rib spacing	52	mm
Number of ribs	6	Number

### 3. NSGA-2-Based Multi-Objective Parameterization Optimization of Cylindrical Pressure-Resistant Shells

#### 3.1. Sensitivity Analysis of Parameters for Cylindrical Shells with Inner Rib Reinforcement under High Pressure

The primary design variables in this section are the thickness of the pressure-resistant shell ( $t$ ), the rib thickness ( $b_1, b_2, b_3, b_4, b_5, b_6$ ), and the rib spacing,  $L$ , which are based on the internal rib stiffness adjustment method suggested in the previous text. The rib thickness can be calculated using the internal rib stiffness adjustment method described in the preceding text, which is  $b_1 = b_6, b_2 = b_5, \text{ and } b_3 = b_4$ . This article takes the thickness  $h$  of the end caps as an optimization parameter and includes the end caps at both ends of the pressure-resistant shell in the optimized model, in addition to the parameters mentioned above. We simultaneously set the Mises stress  $S$ , shell mass  $M$ , and buckling characteristic value  $Q$  as the output responses.

These are the initial values of the design variables:  $t = 5 \text{ mm}, h = 15 \text{ mm}, b_1 = b_6 = 9.1 \text{ mm}, b_2 = b_5 = 9.91 \text{ mm}, b_3 = b_4 = 10.78 \text{ mm}, L = 52 \text{ mm}$ . Table 10 illustrates the range of design variables pertaining to pressure-resistant shells.



**Table 10.** Design variable range for pressure resistant shell.

Design Variable	$t/mm$	$h/mm$	$b_1/mm$	$b_2/mm$	$b_3/mm$	$L/mm$
Initial value	15	15	9.1	9.91	10.78	52
Value range	7.5~17.5	10~25	5~15	5.5~15.5	6~16	40~58

For sensitivity analysis, we employed a global sensitivity analysis method based on variance. This paper used an optimal Latin sampling experiment to extract samples consistently and comprehensively. ANSYS Workbench was utilized to conduct simulation analysis after 60 sample points were uniformly extracted for every design variable. The experimental setup for sensitivity analysis was as follows: the mesh was set as a hexahedral mesh with a mesh size of 1 mm. The convergence process of the mesh was automatically determined by the program, and the fixed constraints were at the circular rings on both sides of the cylindrical surface. The pressure was set to 10 MPa on both sides of the cylindrical surface. Figures 12–15 display the obtained sensitivity relationships for each design variable. The sensitivity of each design variable to the output is shown in Table 11.

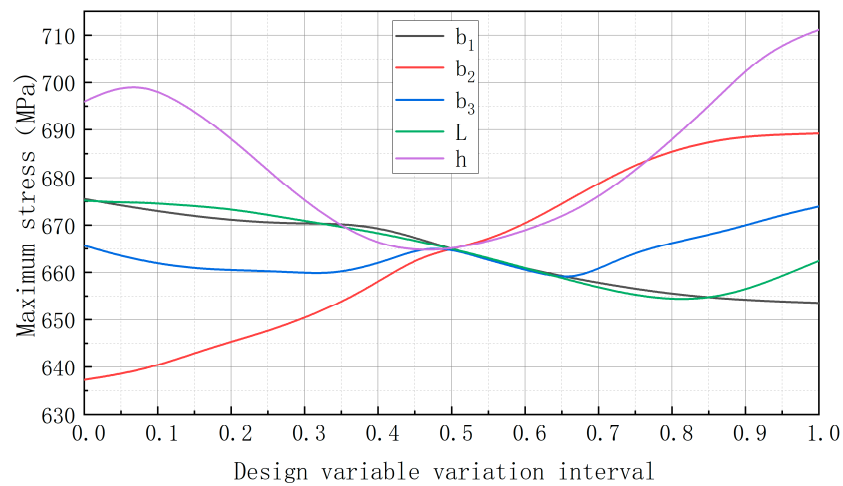


**Figure 12.** Sensitivity relationship curve between design variables and stress.

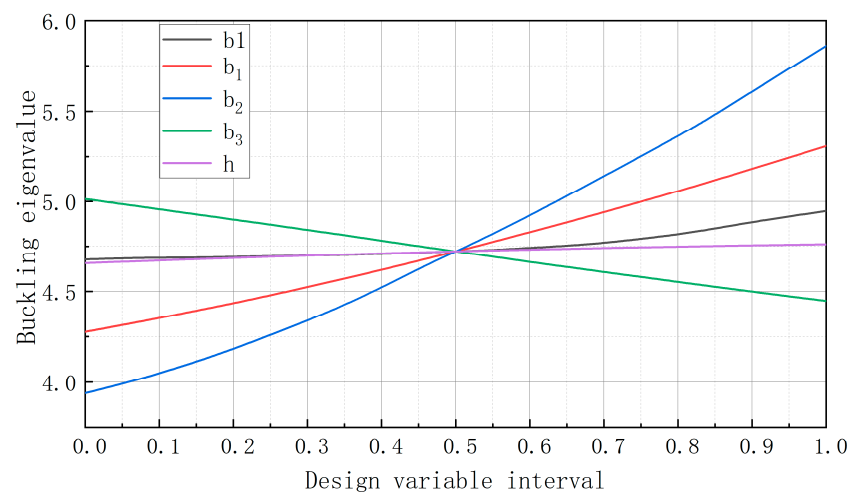


**Figure 13.** Sensitivity relationship curve between design variables and buckling characteristic values.

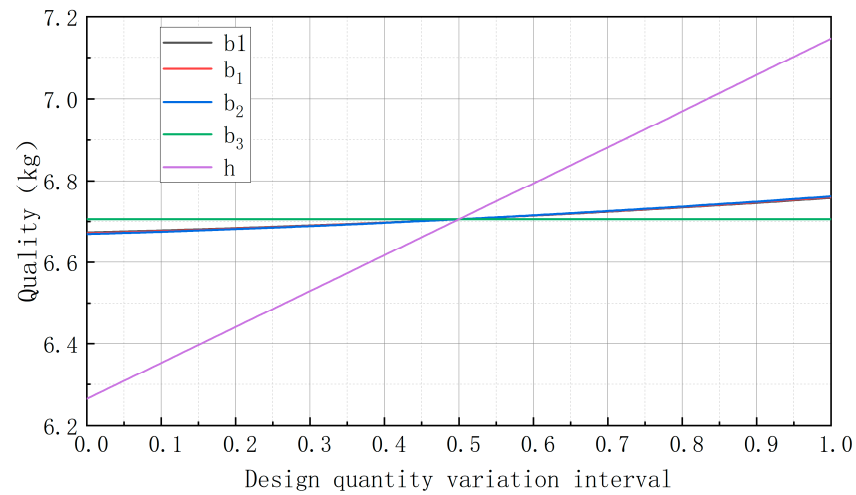


Figure 14. Sensitivity relationship curve between design variables and quality.

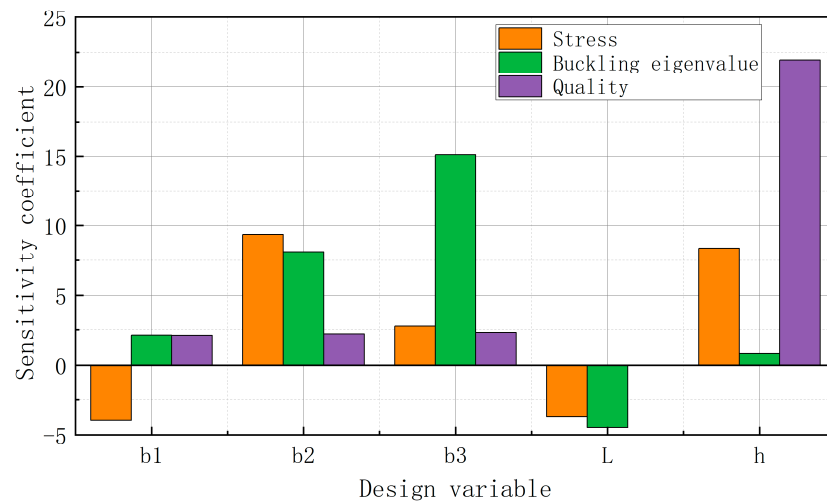


Figure 15. Bar chart showing the sensitivity relationship between design variables and various output responses.

Table 11. Sensitivity of each design variable to the corresponding output.

Response Sensitivity	<i>t</i>	<i>b</i> <sub>1</sub>	<i>b</i> <sub>2</sub>	<i>b</i> <sub>3</sub>	<i>L</i>	<i>h</i>
Stress	0.6983	0.0397	0.0937	0.0275	0.0371	0.0837
Buckling	0.7105	0.0212	0.0813	0.1511	0.0446	0.0827
Quality	0.7168	0.0209	0.0219	0.02293	0	0.2196

The images and tables above make it easy to determine that, at 0.6983, 0.7105, and 0.7168, respectively, the shell thickness *t* has the highest sensitivity to stress, buckling, and mass. With a stress ratio of 0.0837, the end cap’s thickness *h*’s sensitivity to quality is a specific relationship. The most notable rib width is *b*<sub>3</sub>, which also explains a portion of the sensitivity in buckling and stress (0.1511 in buckling and 0.0623 in stress). With 0.0937 in stress and 0.0813 in buckling, *b*<sub>2</sub> also has some effect in these areas.

### 3.2. Multi-Objective Parameterized Optimization Process

Generally speaking, multi-objective optimization is an optimization technique that has several optimization goals that, to varying degrees, directly impact the objective

function. Determining the design variables, constraints, and objective function is the first step towards creating a mathematical model of the objective function [33].

Using the sensitivity analysis of each parameter from the previous text as a guide, this article will optimize each parameter by choosing multiple appropriate parameters to be used as design variables for multi-objective optimization.

Meanwhile, the pressure-resistant shell must also adhere to the pertinent clauses of the “Classification and Construction Specification for Submarine Systems and Submarines” and confirm the circumferential normal stress  $\sigma_2^0$  on the middle surface of the shell plate at the midpoint of the two ribs, the axial normal stress  $\sigma_f$  representing the ribs, the critical pressure of instability  $P_{cr}$ , and the axial normal stress  $\sigma_1'$  at the edge of the ribs. Thus, the following are the constraint conditions:

$$y = f(x_1, x_2, \dots, x_s), X = (x_1, x_2, \dots, x_s) \in C^S \tag{18}$$

$$\begin{cases} \sigma_2^0 = -\frac{PR}{t}(1 - \varepsilon_4) \leq 0.85\sigma_s \\ \sigma_1' = -\frac{PR}{t}(0.56 \mp \varepsilon_2) \leq 1.15\sigma_s \\ \sigma_f = -\frac{PR}{t}(1 - \varepsilon_1)(1 - 0.5\mu) \leq 0.6\sigma_s \\ P_{cr} \geq 1.5P \end{cases} \tag{19}$$

Here, we integrate the constraints, goal functions, and design variables that were suggested in the earlier text. For pressure-resistant shells, the following multi-objective optimization model can be created:

$$\begin{cases} g_k(X) - h_\rho(X) \leq 0 \text{ or } \geq 0, k, \rho \in (1, 2, 3, \dots) \\ X = [x_1 \ x_2 \ x_3 \ \dots \ x_i \ x_n]^T \ (n \leq N) \ (x_{imin} \leq N \leq x_{imax}) \\ F(X) = [f_1(X) \ f_2(X) \ f_3(X) \ \dots \ f_i(X) \ \dots \ f_m(X)] \\ \min F(X) = \min f_i(X) \ (i = 1, 2, 3, \dots, m) \end{cases} \tag{20}$$

where

- (a)  $X$ —a set of design variables;
- (b)  $h_\rho(X)$ —the function of boundary conditions;
- (c)  $g_\rho(X)$ —the function of constraint conditions;
- (d)  $F(X)$ —the objective function for optimization.

### 3.3. Analysis of Optimization Results

Particle swarm optimization, genetic algorithms, ant colony algorithms, and other optimization algorithms are currently popular multi-objective optimization techniques. Apart from the commonly used algorithms previously mentioned, another enhanced version of genetic algorithms is the second-generation fast non-dominated genetic algorithm (NSGA-2). NSGA-2 offers several advantages over traditional optimization algorithms, including quick convergence, quick computation, and good global search performance. For every optimized data set, the second-generation fast non-dominated genetic algorithm will be chosen as the optimization algorithm in this article. The NSGA-2 flowchart is displayed in Figure 16.

A total of thirty sets of sample points were chosen for the experiment through uniform sampling within each design variable’s value range using the best Latin hypercube experiment technique. The 30 sets of sample points were then simulated and examined using ANSYS Workbench. Table 12 displays the pertinent sample points and output response values.

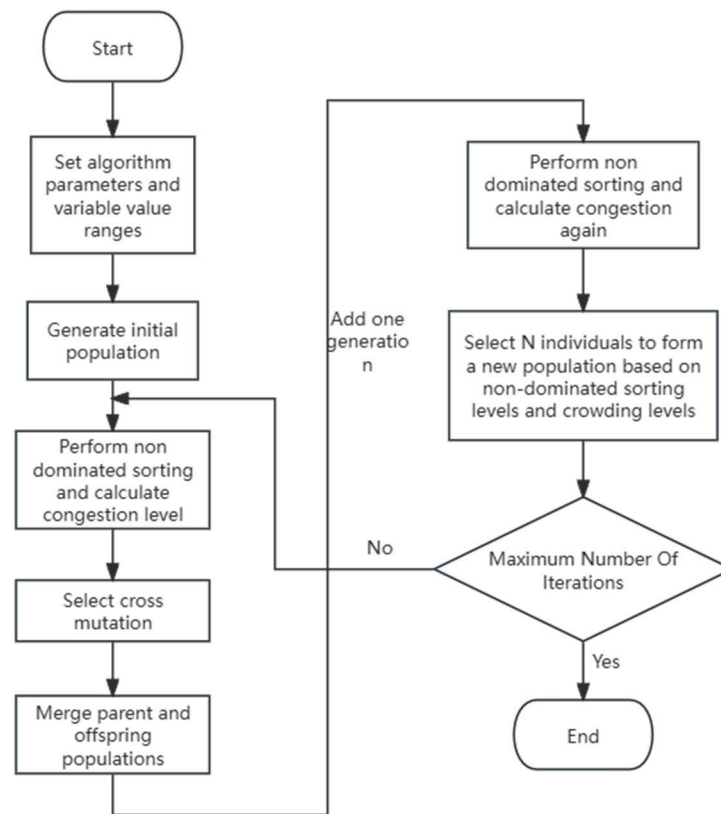


Figure 16. NSGA-2 process diagram.

Table 12. Sample points and output response values.

Group	Shell Thickness $t/mm$	Rib Width $b_1/mm$	Rib Width $b_2/mm$	Rib Width $b_3/mm$	Rib Spacing $L/mm$	End Cover Thickness $h/mm$	Stress/MPa	Buckling Characteristic Value $Q$	Quality $M/kg$
1	7.75	6.75	12.25	10.08	45.55	22.38	935.43	1.501	5.604
2	8.08	12.25	13.75	11.92	52.15	17.13	878.71	1.537	5.634
3	8.42	9.25	8.58	8.08	48.55	21.88	850.06	2.827	5.954
4	8.75	14.25	10.75	13.92	49.15	24.88	871.17	2.162	5.861
5	9.08	12.08	14.25	8.25	49.45	18.88	820.57	2.121	5.859
6	9.42	9.42	5.75	14.75	48.85	22.63	775.31	2.552	5.749
7	9.75	7.58	6.92	10.25	46.45	10.13	795.27	2.252	5.795
8	10.08	11.42	8.25	10.42	40.15	20.38	858.23	2.315	5.696
9	10.42	7.75	11.92	6.75	48.25	22.13	760.14	3.096	5.721
10	10.75	13.75	11.08	11.75	43.45	12.63	704.39	3.83	6.137
11	11.08	5.08	8.75	14.25	42.85	24.13	688.07	4.352	5.983
12	11.42	8.75	6.25	10.58	41.35	13.88	686.14	4.713	6.213
13	11.75	10.08	14.75	7.08	50.35	23.63	690.13	4.226	6.574
14	12.08	13.92	7.92	7.75	50.65	23.38	842.72	4.147	6.565
15	12.42	11.58	12.42	7.25	44.35	22.88	603.13	4.274	6.787
16	12.75	6.92	11.25	15.92	56.65	18.63	650.92	4.338	7.097
17	13.08	5.25	13.58	15.25	51.55	16.38	817.61	4.84	7.210
18	13.42	6.42	12.92	8.42	46.15	19.38	706.07	4.585	7.340
19	13.75	11.08	9.92	12.75	44.95	14.13	604.79	5.735	6.803
20	14.08	9.08	7.42	13.58	53.05	12.38	599.77	5.392	7.528
21	14.42	8.25	6.08	7.92	55.45	17.88	556.99	6.152	7.001
22	14.75	6.08	14.08	10.92	41.65	11.13	571.28	5.995	7.569
23	15.08	8.92	10.08	10.75	52.75	12.88	555.68	7.101	7.579
24	15.42	7.42	9.42	13.42	42.55	16.13	543.09	6.995	7.027
25	15.75	12.42	9.75	6.58	46.75	17.38	556.50	7.419	7.897
26	16.08	14.75	7.25	13.08	44.05	19.88	563.36	7.652	7.791
27	16.42	10.42	11.42	15.58	41.95	21.38	528.72	8.62	8.263

Table 12. Cont.

Group	Shell Thickness <i>t</i> /mm	Rib Width <i>b</i> <sub>1</sub> /mm	Rib Width <i>b</i> <sub>2</sub> /mm	Rib Width <i>b</i> <sub>3</sub> /mm	Rib Spacing <i>L</i> /mm	End Cover Thickness <i>h</i> /mm	Stress/MPa	Buckling Characteristic Value <i>Q</i>	Quality <i>M</i> /kg
28	16.75	14.42	7.58	15.42	47.65	24.63	523.15	8.875	8.066
29	17.08	9.92	7.08	9.75	49.75	23.13	574.69	10.159	7.962
30	17.42	5.58	14.42	8.92	45.25	23.88	500.12	10.317	8.286

Currently, multi-objective optimization results are typically assessed using four indicators: relative absolute maximum error, relative average error, root mean square error, and coefficient of certainty  $R^2$ . The degree to which variable  $X$  in the equation explains variable  $Y$  is indicated by the coefficient of certainty, or  $R^2$ . The explanatory power increases with the distance between  $R^2$  and 1. The prediction accuracy is represented by the relative absolute maximum error, relative mean error, and root mean square error. The prediction is more accurate the closer the error value is to 0. The coefficient of certainty  $R^2$  and the relationship are as follows:

$$R^2 = \frac{\sum_{i=1}^{n_i} (\hat{y}_i - \bar{y}_i)^2}{\sum_{i=1}^{n_i} (y_i - \bar{y}_i)^2} \tag{21}$$

where  $N$ —the number of test sample points;

$\hat{y}_i$ —the predicted values of the model;

$\bar{y}_i$ —the mean of the experimental response value;

$y_i$ —the response value of the model.

The comparisons between the simulation values and the expected response values for each output are displayed in Figures 17–19.

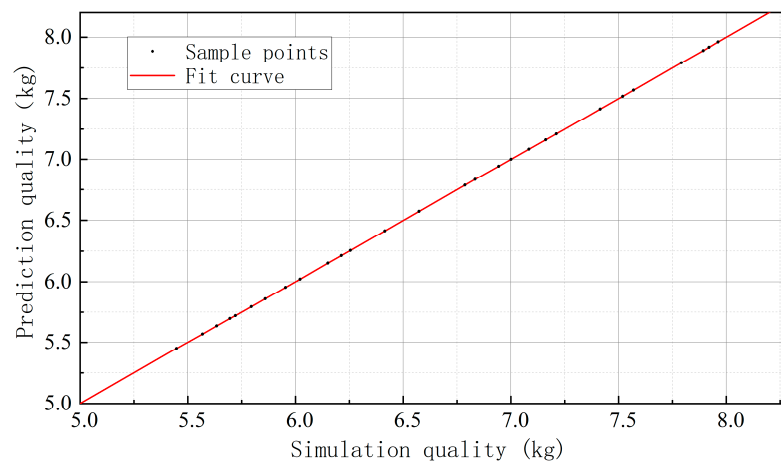
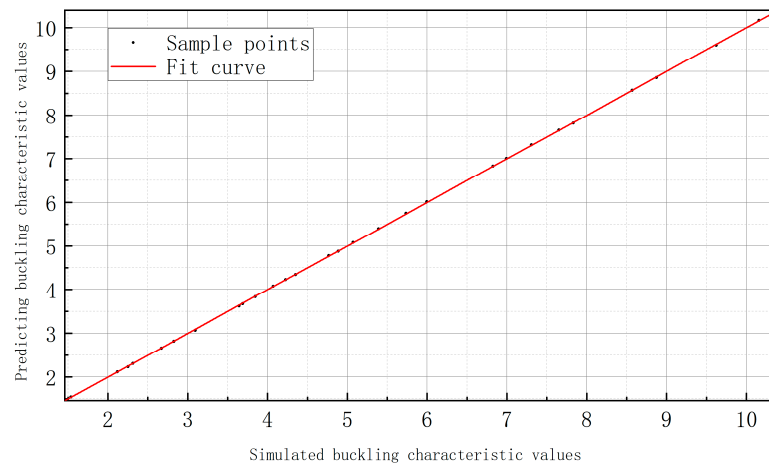


Figure 17. Comparison between predicted and simulated stress values for pressure-resistant shells.

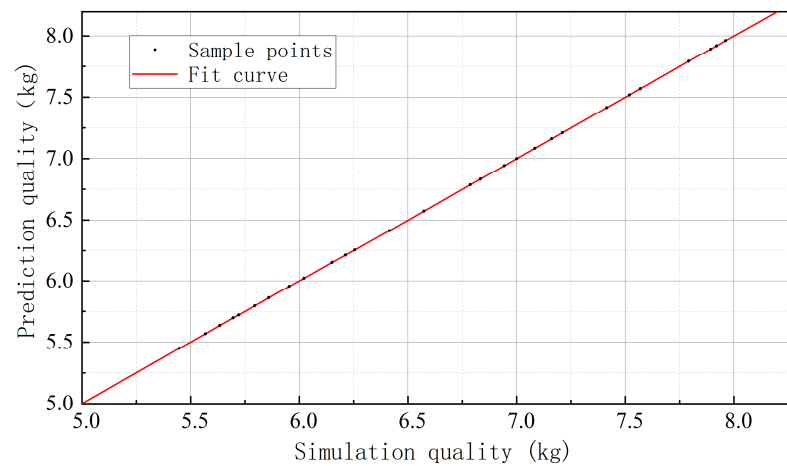
A variety of indicators for evaluating the approximate model’s accuracy can be obtained using Workbench (see Table 13).

Table 13. Approximation model accuracy evaluation indicators.

Evaluating Indicator	Stress	Buckling Eigenvalue	Quality
Determination coefficient $R^2$	0.99657	0.99997	0.99999
Root mean square error	0.09775	0.01427	$1.232 \times 10^{-10}$
Relative maximum absolute error (%)	4.7582	1.6343	0.092175
Relative average absolute error (%)	4.6245	0.43933	0.0096425



**Figure 18.** Comparison between predicted and simulated buckling characteristic values of pressure-resistant shells.



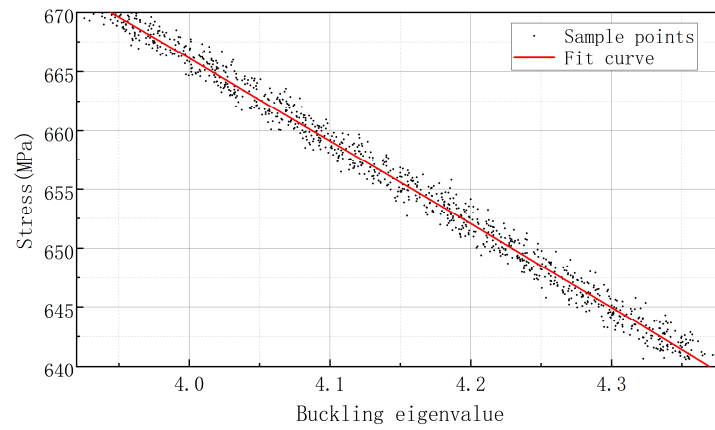
**Figure 19.** Comparison between predicted and simulated values of pressure shell quality.

Table 13 shows that the model’s accuracy is good even though the stress values on the two evaluation indicators—relative maximum absolute error and relative average absolute error—are slightly higher but still fall within the permitted range of model error. Stress constraint conditions must be set when optimizing pressure-resistant shells multi-objectively with ANSYS Workbench. In compliance with “Submarine Strength” regulations, submarines delving deeper than two thousand meters are required to have a minimum safety factor greater than 1.5. With a safety factor of  $\eta = 1.5$ , the maximum stress limit established in this article is  $[\sigma] = \sigma_S / \eta \approx 650$  MPa. The target is the maximum buckling characteristic value and the minimum mass. After obtaining the candidate design points (A~E), the pertinent parameters were determined, as displayed in Table 14. Simultaneously, the response values’ trend of changes was also acquired, as Figure 20 illustrates.

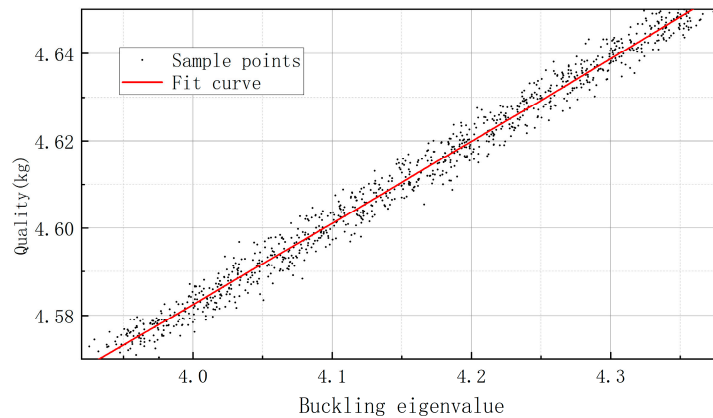
Table 15 displays the pertinent findings from the comparison of the five candidate points mentioned above with the original prototype. The quality difference between each candidate point and the prototype is indicated by the symbol  $\Delta M$ .

**Table 14.** Candidate points for optimizing pressure-resistant shells.

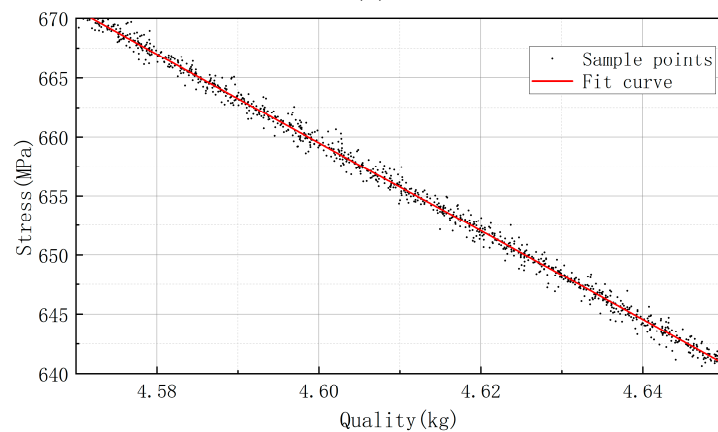
Design Variable	Shell Thickness $t/mm$	Rib Width $b_1/mm$	Rib Width $b_2/mm$	Rib Width $b_3/mm$	Rib Spacing $L/mm$	End Cover Thickness $h/mm$
Initial value	15	9.1	9.91	10.78	52	15
A	11.000	5.497	5.521	15.654	47.248	13.465
B	11.093	6.933	5.679	13.272	47.329	13.145
C	11.019	9.816	5.525	12.861	45.914	13.062
D	11.066	8.560	5.884	13.300	45.520	13.137
E	10.935	11.278	5.618	15.467	44.537	13.113



(a)



(b)



(c)

**Figure 20.** The trends of changes between different response values: (a) stress–buckling characteristic value; (b) quality–buckling characteristic value; (c) stress–quality.

**Table 15.** Comparison results between each candidate point and the original prototype.

Responses	Stress	Buckling Eigenvalue	Shell Mass (with End Cap)/kg	$\Delta M/kg$
Original prototype	549.33	5.8562	7.237	—
A	644.26	4.3677	6.0108	1.2262
B	646.73	4.3464	5.9988	1.2382
C	649.12	4.3051	5.9878	1.2492
D	647.17	4.3477	6.0029	1.2341
E	645.88	4.3968	6.0116	1.2254

It is evident from Table 16. that every design point achieved a weight reduction of more than 1.2 kg in comparison to the original prototype, with candidate point C reaching the greatest weight reduction of 1.2492 kg. Regarding maximum stress, each candidate point’s maximum stress has grown considerably when compared to the original prototype, but it is still quite near to the predetermined 650 MPa, suggesting that all of the material has been used. Every potential point is above 4.3 in the characteristic buckling value, indicating that the stability satisfies the necessary conditions. This article will use candidate point C as the final design scheme for the pressure-resistant shell parameters, even though candidate points A through E meet the various performance requirements of the pressure-resistant shell. Candidate point C achieves the most weight reduction, reaching 1.2492 kg, accounting for 17.26% of the original pressure-resistant shell.

The final values of the various parameters of the pressure-resistant shell obtained are shown in Table 16. It is necessary to round off the various parameters of candidate point C due to the accuracy of the machining. Figure 21 displays the schematic diagram of the pressure-resistant shell structure.

**Table 16.** Final parameters of pressure-resistant shell after rounding processing.

Design Variable	Shell Thickness $t/mm$	Rib Width $b_1/mm$	Rib Width $b_2/mm$	Rib Width $b_3/mm$	Rib Spacing $L/mm$	End Cover Thickness $h/mm$
Numerical value	11	10	6	13	45	13

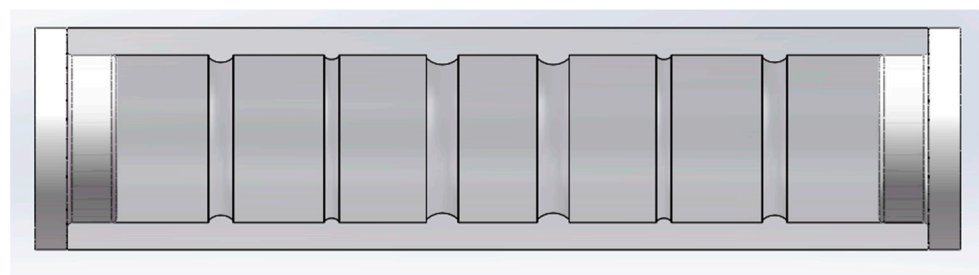


**Figure 21.** Schematic diagram of pressure-resistant housing structure.

#### 4. Conclusions

In order to increase the critical instability pressure of pressure-resistant shells in settings at tens of thousands of meters of water depth, this article suggests combining the Liz method with an internal rib stiffness adjustment technique. By ensuring that the critical instability pressure met the working conditions, the shape of the inner ribs was optimized using the orthogonal topology optimization method in order to further achieve lightweight design. Based on this, the pressure-resistant shell’s multi-objective optimization design was ultimately optimized using a second-generation fast non-dominated genetic algorithm.



The pressure-resistant shell was then further treated to make it lighter. The article's primary findings are listed below:

- (1) In order to optimize deep-sea high-pressure structural layers, this article suggests a lightweight design approach for pressure-resistant devices in high-pressure deepwater environments that satisfies the non-unstable requirement.
- (2) The determined pressure-resistant shell was subjected to internal rib stiffness adjustment using the proposed internal rib stiffness adjustment method in conjunction with the Liz method. Through the use of ANSYS 2023 R1 simulation software, this process was compared and verified with traditional uniform rib addition. There was a 9.65 MPa increase in the critical instability pressure following the modification of the internal rib stiffness and an improvement in the pressure-resistant shell's overall anti-instability performance.
- (3) Titanium alloy TB9 material is unique in a high-pressure setting. An orthogonal topology optimization method was proposed for the inner rib section in order to reduce material costs. This method yielded the optimal inner rib arch section shape and resulted in a 106.8 g weight reduction. Based on this, a sensitivity analysis was performed on the pressure-resistant shell, and a second-generation fast non-dominated genetic algorithm was applied to carry out additional multi-objective optimization. After determining the pressure-resistant shell's ideal structural parameters, 1.2492 kg of weight—or 17.26% of the original pressure-resistant shell—was reduced.

This article generally suggests a lightweight design approach for pressure-resistant devices in high-pressure water depth environments that satisfy the stability requirement, as well as an internal rib adjustment method to enhance their anti-instability ability. This offers a fresh method for optimization for lightweighting and strengthening the stability of deep-sea high-pressure-resistant structural layers, creating a process method that is both scientifically and engineeringly significant.

**Author Contributions:** Conceptualization, Y.H. and H.M.; methodology, X.W.; software, X.W.; validation, Z.L., Y.Y. and H.M.; formal analysis, X.W.; investigation, Z.L.; resources, H.M.; data curation, Y.Y.; writing—original draft preparation, X.W.; writing—review and editing, Y.H.; visualization, Z.L.; supervision, Y.Y.; project administration, H.M.; funding acquisition, Y.H. All authors have read and agreed to the published version of the manuscript.

**Funding:** This research was funded by National Key R&D Program Projects, grant number 2022YFC3104000.

**Institutional Review Board Statement:** The study did not require ethical approval.

**Informed Consent Statement:** Not applicable.

**Data Availability Statement:** Data available on request.

**Conflicts of Interest:** The authors declare no conflicts of interest.

## References

1. Ramadass, G.A.; Vedachalam, N.; Ramesh, S.; Sathianarayanan, D.; Subramanian, A.N.; Ramesh, R.; Chowdhury, T.; Pranesh, S.B.; Atmanand, M.A. Challenges in developing deep-water human occupied vehicles. *Curr. Sci.* **2020**, *118*, 1687–1693. [[CrossRef](#)]
2. Ramadass, G.A.; Ramesh, S.; Vedachalam, N.; Subramanian, A.N.; Sathianarayanan, D.; Ramesh, R.; Harikrishnan, G.; Chowdhury, T.; Jyothi, V.B.N.; Pranesh, S.B.; et al. Unmanned underwater vehicles. *Curr. Sci.* **2020**, *118*, 1681–1686. [[CrossRef](#)]
3. Joo, M.G.; Qu, Z. An autonomous underwater vehicle as an underwater glider and its depth control. *Int. J. Control Autom. Syst.* **2015**, *13*, 1212–1220. [[CrossRef](#)]
4. Jaffre, F.; Littlefield, R.; Grund, M.; Purcell, M. Development of a New Version of the REMUS 6000 Autonomous Underwater Vehicle. In Proceedings of the OCEANS 2019—Marseille, Marseille, France, 17–20 June 2019.
5. Purcell, M.; Gallo, D.; Packard, G.; Dennett, M.; Rothenbeck, M.; Sherrell, A.; Pascaud, S. Use of REMUS 6000 AUVs in the search for the Air France Flight 447. In Proceedings of the OCEANS'11 MTS/IEEE KONA, Waikoloa, HI, USA, 19–22 September 2011.
6. Roper, D.; Harris, C.A.; Salavasidis, G.; Pebody, M.; Templeton, R.; Prampart, T.; Kingsland, M.; Morrison, R.; Furlong, M.; Phillips, A.B.; et al. Autosub Long Range 6000: A Multiple-Month Endurance AUV for Deep-Ocean Monitoring and Survey. *IEEE J. Ocean. Eng.* **2021**, *46*, 1179–1191. [[CrossRef](#)]

7. McPhail, S. Autosub6000: A Deep Diving Long Range AUV. *J. Bionic Eng.* **2009**, *6*, 55–62. [[CrossRef](#)]
8. Yang, S.; Wang, Y.; Liang, Y.; Wang, S.; Zhang, L.; Yang, M. Optimization design of neutrally buoyant hull for underwater gliders. *Ocean. Eng.* **2020**, *209*, 107512. [[CrossRef](#)]
9. Prasanna, A.S.; Raju, K.K.S.; Ramji, K.; Satish, P. Free Vibration, Buckling and Design Optimisation of Composite Pressure Hulls. *Mater. Today Proc.* **2017**, *4*, 7381–7387. [[CrossRef](#)]
10. Imran, M.; Shi, D.; Tong, L.; Waqas, H.M.; Muhammad, R.; Uddin, M.; Khan, A. Design Optimization and Non-Linear Buckling Analysis of Spherical Composite Submersible Pressure Hull. *Materials* **2020**, *13*, 2439. [[CrossRef](#)] [[PubMed](#)]
11. Fathallah, E.; Qi, H.; Tong, L.; Helal, M. Design Optimization of Composite Elliptical Deep-Submersible Pressure Hull for Minimizing the Buoyancy Factor. *Adv. Mech. Eng.* **2014**, *2014*, 987903. [[CrossRef](#)]
12. Shi, D.; Tong, L.; Elahi, A.; Waqas, H.M.; Uddin, M.; Imran, M. Multi-objective design optimization of composite submerged cylindrical pressure hull for minimum buoyancy factor and maximum buckling load capacity. *Def. Technol.* **2021**, *17*, 1190–1206.
13. Wang, C.; Yang, M.; Wang, Y.; Ren, M.; Wang, Z.; Yang, S. Design and optimization of cylindrical hull with non-uniform arch ribs for underwater gliders based on approximate model and experiments. *Ocean. Eng.* **2022**, *259*, 111831. [[CrossRef](#)]
14. Liu, H.; Li, B.; Yang, Z.; Hong, J. Topology optimization of stiffened plate/shell structures based on adaptive morphogenesis algorithm. *J. Manuf. Syst.* **2017**, *43*, 375–384. [[CrossRef](#)]
15. Foryś, P. Optimization of cylindrical shells stiffened by rings under external pressure including their post-buckling behaviour. *Thin-Walled Struct.* **2015**, *95*, 231–243. [[CrossRef](#)]
16. Ghasemi, A.R.; Hajmohammad, M.H. *Minimum-Weight Design of Stiffened Shell under Hydrostatic Pressure by Genetic Algorithm*; Techno-Press: Daejeon, Republic of Korea, 2015.
17. Shimoda, M.; Okada, T.; Nagano, T.; Shi, J.-X. Free-form optimization method for buckling of hull structures under out-of-plane and in-plane shape variations. *Struct. Multidiscip. Optim.* **2016**, *54*, 275–288. [[CrossRef](#)]
18. Wu, H.; Yan, Y.; Yan, W.; Liao, B. Adaptive Approximation-based Optimization of Composite Advanced Grid-stiffened Cylinder. *Chin. J. Aeronaut.* **2010**, *23*, 423–429.
19. Mehrabani, M.M.; Jafari, A.A.; Azadi, M. Multidisciplinary optimization of a stiffened hull by genetic algorithm. *J. Mech. Sci. Technol.* **2012**, *26*, 517–530. [[CrossRef](#)]
20. Akl, W.; Ruzzene, M.; Baz, A. Optimal design of underwater stiffened hulls. *Struct. Multidiscip. Optim.* **2002**, *23*, 297–310. [[CrossRef](#)]
21. Sofiyev, A.H.; Fantuzzi, N. Stability analysis of shear deformable inhomogeneous nanocomposite cylindrical shells under hydrostatic pressure in thermal environment. *Materials* **2023**, *16*, 4887. [[CrossRef](#)]
22. Wang, M.; Liu, F.; Zhang, J. Collaborative optimization of a composite pressure cylindrical shell based on dynamic penalty functions. *Ocean. Eng.* **2024**, *309*, 118542. [[CrossRef](#)]
23. Yang, Z.; Zhang, X.; Pan, G.; Xu, Y. Buckling and strength failure for unstiffened and ring-stiffened composite shells. *Ocean. Eng.* **2023**, *278*, 114513. [[CrossRef](#)]
24. Zhang, X.; Sun, J.; Wu, R.; Peng, Y. Buckling performance of inner corrugated pressure shells under external hydrostatic pressure. *Ocean. Eng.* **2023**, *288*, 115963. [[CrossRef](#)]
25. Zhang, Y.; Chen, Y.; Yun, L.; Liang, X. Mechanical performance of bio-inspired bidirectional corrugated sandwich pressure shell under external hydrostatic pressure China. *Ocean. Eng.* **2024**, *38*, 297–312. [[CrossRef](#)]
26. Wang, B.; Yang, M.; Zeng, D.; Hao, P.; Li, G.; Liu, Y.; Tian, K. Post-buckling behavior of stiffened cylindrical shell and experimental validation under non-uniform external pressure and axial compression. *Thin-Walled Struct.* **2021**, *161*, 107481. [[CrossRef](#)]
27. Wei, R.; Shen, K.; Pan, G.; Li, Z. Experimental study on buckling behavior of composite cylindrical shells with and without circular holes under hydrostatic pressure. *Compos. Struct.* **2023**, *322*, 117434. [[CrossRef](#)]
28. Cheng, Y. Structural Optimization Design of the Pressure Hull Based on Nonuniform Ring-Frames Theory. Master's Thesis, Harbin Engineering University, Harbin, China, 2012.
29. Feng, Y. HXJ180 Marine Workover Machine Derrick Lightweighting Study. Master's Thesis, Yangtze University, Jingzhou, China, 2023.
30. Du, Y.-X.; Wang, W.; Tian, Q.-H. Optimal Designs of Parameters of Structural Topology Optimization by Orthogonal Experiment. *Mach. Des. Res.* **2011**, *27*, 14–17.
31. Yang, R.; Tang, P.; Ni, X.; Xiao, L.; Zhao, H. Structural Analysis and Design of an Electric Bus Frame. *J. Yancheng Inst. Technol. (Nat. Sci. Ed.)* **2022**, *35*, 30–37.
32. Ren, S.; Gao, A.; Zhang, Y.; Han, W. Finite element analysis and topology optimization of folding mechanism of six-rotor plant protection UAV. *J. Chin. Agric. Mech.* **2021**, *42*, 53–58+194.
33. Yang, S. Structure Design and Optimization of Pressure Cabin of Underwater Vehicle. Master's Thesis, Jiangxi University of Science and Technology, Ganzhou, China, 2020.

**Disclaimer/Publisher's Note:** The statements, opinions and data contained in all publications are solely those of the individual author(s) and contributor(s) and not of MDPI and/or the editor(s). MDPI and/or the editor(s) disclaim responsibility for any injury to people or property resulting from any ideas, methods, instructions or products referred to in the content.